Journal of Hazardous Materials 502 (2026) 140623

Contents lists available at ScienceDirect

Journal of Hazardous Materials

journal homepage: www.elsevier.com/locate/jhazmat

Integration of transition metal onto alginate activated carbon (M-AAC) for enhancing molybdate electro-adsorption

Yu-Jen Shih [a,*], Zhi-Lun Wu [a], Chi-Yun Shen [a], Chin-Pao Huang [b]

[a] Institute of Environmental Engineering, National Sun Yat-sen University, Taiwan
[b] Department of Civil and Environmental Engineering, University of Delaware, Newark, DE 19716, USA

HIGHLIGHTS

- Mo recovery was achieved via electro-sorption in a MCDI system.
- Alginate-derived carbon activated with transition metals were prepared as electrodes.
- Pseudocapacitive characteristics of M-AAC facilitated Mo uptake under applied potential.
- Co-AAC delivered the highest adsorption capacity and stable cycling performance.
- DFT calculations supported the preferential adsorption of molybdate on Co-AAC.

GRAPHICAL ABSTRACT

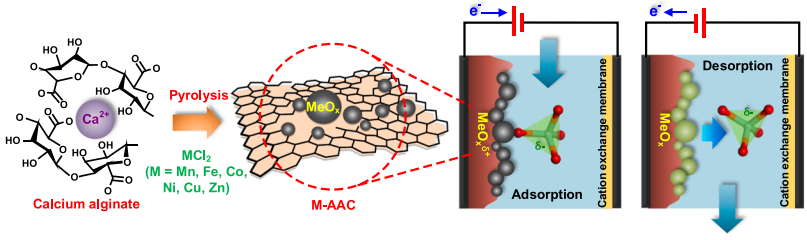

ARTICLE INFO

Keywords:
Molybdate
Electro-sorption
Alginate-derived carbon
Pseudocapacitance, Co_3O_4

ABSTRACT

Molybdenum (Mo) in industrial effluents emerges both an environmental concern and a valuable recyclable resource. In this study, metal oxide-alginate activated carbons (M-AAC, M = Mn, Fe, Co, Ni, Cu, and Zn) were synthesized for Mo recovery in a membrane capacitive deionization (MCDI) system. Pyrolysis of alginate precursors significantly enhanced the effective surface area and dispersion of metal oxides within mesoporous carbon textures. The pseudocapacitive transformation of metal oxides contributed to charge storage, which increased the adsorption capacity for molybdate oxyanions under anodic potentials. Among the electrodes, Co-AAC demonstrated the highest Mo adsorption capacity (72 mg-Mo g^{-1}). Raman spectroscopy and free energy calculations indicated that Co_3O_4 active sites promoted molybdate uptake via multi-dentate complexation. At + 1.0 V (vs. RHE) and neutral pH, the Co-AAC electrode achieved excellent cycling stability for molybdate electro-sorption/desorption, along with strong selectivity over commons anions present in real water samples.

1. Introduction

Molybdenum (Mo) is an essential trace element for both plants and animals, primarily serving as a micronutrient in plant nutrition due to its relatively low natural abundance in soils. However, elevated Mo concentrations in aquatic environments can lead to toxicity, posing adverse health effects in humans, such as loss of appetite, fatigue, diarrhea, and anemia [1]. To address these concerns, the World Health Organization (WHO) has set a guideline limit of 70 μg-Mo/L for drinking water, while the United States Environmental Protection Agency (US

* Corresponding author.
E-mail address: yjshih@mail.nsysu.edu.tw (Y.-J. Shih).

https://doi.org/10.1016/j.jhazmat.2025.140623
Received 21 September 2025; Received in revised form 2 November 2025; Accepted 24 November 2025
Available online 26 November 2025

EPA) recommends a lifetime advisory level of 40 μg-Mo L^{-1} [2,3]. Major sources of Mo contamination in wastewater include electroplating, etching, catalyst production, mining, and fertilizer manufacturing. Given its economic value, various methods have been developed for Mo recovery from industrial effluents, including chemical precipitation, selective extraction, and membrane-based electrodialysis and nanofiltration [4].

As a transition element, Mo exhibits multiple oxidation states ranging from −2 to + 6, with oxyanions being the predominant forms in surface waters. Owing to the close proximity of its first and second acid dissociation constants (pK_{a1} = 3.7, pK_{a2} = 3.9), the deprotonated molybdate ion (MoO_4^{2-}) dominates in neutral solutions [5]. Under acidic conditions and at elevated concentrations (> 10^{-4} M), Mo can also exist as complexes, such as the hepta-molybdate anion ($Mo_7O_{24}^{6-}$) [6]. Therefore, electrostatic-based methods are considered both efficient and economically viable, especially for treating wastewater containing low to moderate Mo concentrations [7]. However, conventional adsorption techniques often suffer from limitations such as poor selectivity, limited reusability, and the production of spent adsorbent, which may hinder their practical application. Electro-sorption – the underlying fundamental of capacitive deionization (CDI) – offers a promising alternative by enabling reversible adsorption and desorption of ionic contaminants through electrode polarity switching [8]. For an ideally polarizable electrodes, the charged surfaces act as capacitors, where counter-ions are electrostatically confined within the electrical double-layer (EDL) structure [9]. CDI systems usually employ electrodes coated with activated carbon or carbon fibers due to their exceptionally high specific surface area – ranging from several hundred to over a thousand m^2 g^{-1} [10]. However, pristine carbon surfaces typically bear negatively charged functional groups, which asymmetrically hinder the adsorption of anionic species [11]. To address this limitation, carbon electrodes are often modified with metal or metal oxide nanoparticles. The redox activity of metal oxides can introduce supplementary structural charges, thereby enhancing CDI capacity when their lattice spacing is well-suited for cation intercalation under cathodic polarization. Moreover, metal oxide surfaces are generally positively charged, and their hydroxyl-rich, redox-active nature promotes oxyanion electro-sorption through ligand exchange and electrostatic attraction. Selective electro-sorption of phosphate, arsenate, and chromate has been demonstrated using Fe-AC, Mn-AC, and Al-AC electrodes [12–14]. In particular, additional charge storage can originate from the battery-like behavior of certain transition metal oxides, such as MnO_2, Co_3O_4, and NiOOH, incorporated into biomass-derived carbon, where desalination proceeds via ion insertion or charge compensation [15,16].

Numerous metal oxide-supported carbon composites have been developed for CDI applications. The tunable pore geometry of the carbonaceous substrate, which accommodates metal active sites, is strongly determined by the biomass precursor [17,18]. Alginate is a natural polysaccharide that constitutes the framework of the algal cell walls. Its functional groups, particularly carboxyl (−COOH) and hydroxyl (–OH), allow for coordination of various metal ions through metal-ligand interactions [19]. When cross-linked with polyvalent cations (e.g. Ca^{2+}, Fe^{3+}), alginate forms water-insoluble hydrogels [20]. These gels can subsequently be dried and pyrolyzed under an inert atmosphere to produce highly homogeneous metal–carbon composites, which serve as excellent adsorbents for a wide range of pollutants. Alginate-based activated carbons have been increasingly explored for the removal of both toxic organic compounds and heavy metals [21–23].

In our previous work, we utilized ZIF-derived carbon, a subclass of metal-organic frameworks (MOFs), for Mo adsorption [24]. The phase transition of metal oxides embedded within the carbon matrix was found to be critical for immobilizing molybdate anions under anodic polarization. Building on the concept, this study synthesizes a series of transition metals-activated alginate carbons (M-AAC, M = Mn, Fe, Co, Ni, Zn, and Cu) hydrothermally, using sodium alginate and metal chlorides as the biomass precursor and activating agents, respectively. The novelty lies in evaluating the influence of metal oxide species on the electrochemical interactions between M-AAC electrodes and molybdate anions. A membrane capacitive deionization (MCDI) cell was constructed to investigate the electro-sorption performance of different M-AAC electrodes. To provide mechanistic insights, the free energies of MoO_4^{2-} adsorption on various metal-carbon sites was calculated via DFT method. Furthermore, the selectivity and practical applicability of Mo electro-sorption were assessed in the presence of competing anions and real water matrices.

2. Methods

The preparation of sodium alginate carbons activated with transition metals (M-AAC, M = Mn, Fe, Co, Ni, Cu, Zn) is illustrated in Fig. 1, with detailed procedures provided in the Supporting Information. Molybdate electro-sorption/desorption experiments using M-AAC anodes, paired with an AAC (activated alginate carbon) cathode, are conducted in a modified membrane capacitive deionization (MCDI) kit, as shown in Fig. S1. In a conventional MCDI setup, cation and anion exchange membranes (CEM and AEM) are placed on the negatively and positively charged electrodes, respectively, allowing counter-ions to migrate from the bulk solution toward the electrodes while blocking co-ions [25]. In this work, a CEM was attached to the cathode to prevent the reduction of MoO_4^{2-} during Mo electrosorption on the anode and potential resorption under polarity reversal. Further, $NaHCO_3$ was used as the anolyte to buffer pH perturbations during Mo electrosorption, whereas the influence of Na_2SO_4 used as the catholyte on competitive adsorption was negligible due to the presence of the CEM.

3. Results and discussion

3.1. Characterization

The SEM image of alginate-derived activated carbon (AAC), shown in Fig. 2a, reveals a typical porous carbon structure characterized by uniform and smooth macro cavities. These macropores serve as open tunnels, facilitating inter-particle transport of pollutants during adsorption. The thermal analysis (TGA/DT) of the calcium alginate precursor in Fig. S2 indicates a three-stage pyrolysis process. Initial weight losses at 150 °C and 260 °C mainly correspond to water evaporation and the decomposition of organic carboxyl/hydroxyl groups, respectively. The final loss at 550 °C associated with combustion of fixed carbon suggests complete carbonization of the precursor, with overall loss exceeding 60 %. Therefore, alginate is further activated with various metal chlorides at 600 °C to form M-AAC, where M = Mn, Fe, Co, Ni, Cu, or Zn. The resulting morphologies of these M-AAC samples are presented in Figs. 2b – 2g, respectively. In the M-AAC composites, nanoparticles and aggregates of metal oxides are thoroughly dispersed over the inner surfaces of the AAC open-pore structure. Notably, elemental analysis reveals that all M-AAC exhibit metal contents ranging from 5 to 10 % atomic percent (approximately 1.5 – 2 wt%), with the exception of Zn-AAC. This consistent metal loading suggests a comparable influence of metal content on the Mo adsorption capacity. Zn-AAC shows a low metal ratio (< 2 at%), likely due to the volatility of Zn species during high-temperature treatment. As $ZnCl_2$ has a low melting point (420 °C), it is commonly used as an activating agent in carbon synthesis. Fig. 2h presents XRD patterns of the M-AAC electrodes. For the pristine AAC, two broad peaks at 26.5° and 43° on AAC are indexed to the (0 0 2) and (1 0 1) planes of a graphitic structure (#75–1621), respectively, confirming the formation of a partially graphitized carbon framework. Upon metal activation, additional peaks corresponding to metal oxides are clearly observed in the M-AAC. The mineral phases are identified as Mn_3O_4 (#80–0382), Fe_2O_3 (#86–0550), Co_3O_4 (#76–1802), NiO (#74–2075), CuO (#71–2027), and ZnO (#79–0207) based on their characteristic diffraction planes on these patterns. The results confirm the incorporation and crystallization of metal oxides on

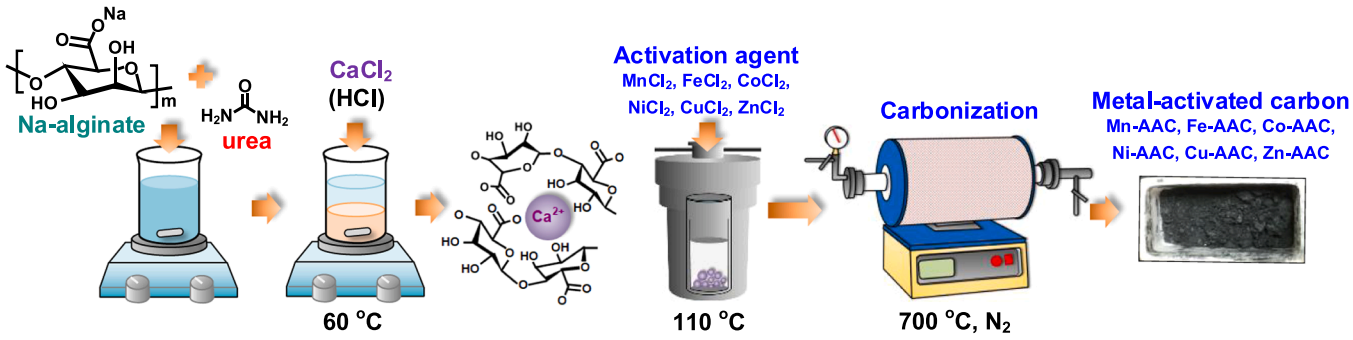

Fig. 1. Procedure of alginate-derived carbon activated with differential metal chlorides (M-AAC).

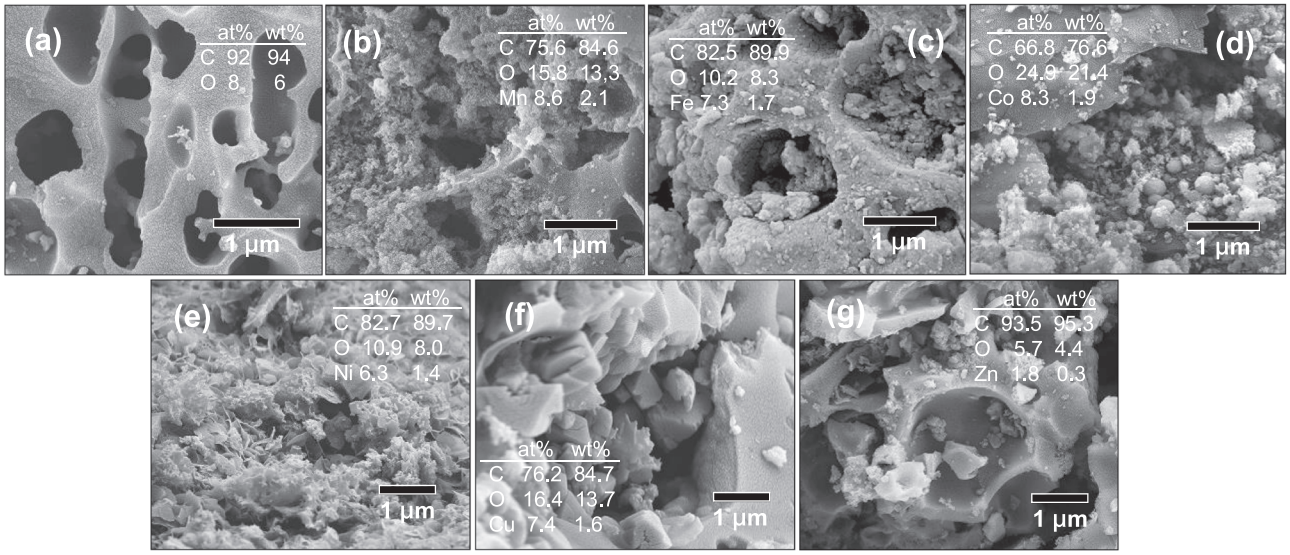

Fig. 2. SEM images and elemental analyses for (a) AAC and M-AAC samples, M = (b) Mn, (c) Fe, (d) Co, (e) Ni, (f) Cu, and (g) Zn. (h) XRD patterns (standard JCPDS cards: ● carbon (75–2078); ◆ Mn_3O_4 (80–0382); ▲ Fe_2O_3 (86–0550); ■ Co_3O_4 (76–1802); ▼ NiO (74–2075); + $Cu(OH)_2$ (71–2027);× ZnO (79–0207)), (i) N_2 adsorption isotherms, and (j) specific surface areas and average pore sizes for different M-AAC samples.

the carbon matrix. The N_2 adsorption – desorption isotherms of the M-AAC samples in Fig. 2i exhibit H3-type hysteresis loops (defined by the International Union of Pure and Applied Chemistry (IUPAC)), which are characteristic of mesoporosity structures [26]. The specific surface area (s.s.a.) flows the order: Zn-AAC (726 m^2 g^{-1}) > Co-AAC (558 m^2 g^{-1}) > Mn-AAC (509 m^2 g^{-1}) > Cu-AAC (223 m^2 g^{-1}) > Ni-AAC (121 m^2 g^{-1}) AAC (43.4 m^2 g^{-1}) > Fe-AAC (9 m^2 g^{-1}), as summarized in Fig. 1j. The high s.s.a. of Zn-AAC is attributed to the volatilization of $ZnCl_2$, which leaves behind a highly porous carbon matrix [27]. Moreover, mesopores dominate the pore size distribution in all M-AAC electrodes, with average diameters of 3 – 15 nm, in contrast to the representative value of 12.2 nm for a pristine AAC sample.

XPS analysis was employed to evaluate the chemical states of M-AAC, with full spectra presented in Fig. S3 and binding energies of transition metals at the corresponding 2p orbitals shown in Fig. 3a. Deconvolution of the $2p_{3/2}$ peaks reveals the ratios of various oxidation states for Mn^{2+} (641 eV)/Mn^{3+} (645 eV), Fe^{2+} (710.5 eV)/Fe^{3+} (712.5), Co^{2+} (781.5 eV)/Co^{3+} (780.2 eV), Ni^{2+} (854.7 eV)/Ni^{3+} (856.5 eV), and Cu^{+} (932.2 eV)/Cu^{2+} (935 eV) as 0.44/0.56, 0.35/0.65, 0.33/0.67, 0.63/0.37, and 0.29/0.71, respectively. These ratios closely match the stoichiometry of mineral phases identified by XRD, confirming the predominant valences of metals in the M-AAC electrodes, while only Zn^{2+} state (1022.2 eV) is observed at Zn 2p, consistent with ZnO precipitation. At the C 1 s orbital (Fig. 3b), four main binding energies – aromatic C═C (284.4 eV), hydroxyl C-OH (285.2 eV), carbonyl C═O (286.2 eV), and carboxylic -COOH (288 eV) – together characterize the carbon substrate [28]. Additional signal at 290.6 eV is attributed to deposited CO_2 or carbonate species. The ratios of these carbon functional groups in M-AAC are summarized in Fig. S4. Incorporation of metals into M-AAC reduces the abundance of oxygenated carbon (C-OH, C═O, and -COOH), indicating that metal/metal oxide nanoparticles preferentially nucleate and grow on these reactive sites. Furthermore, at the O 1 s orbital (Fig. 3c), the peak for adsorbed O_{ads} (531.2 eV) in AAC was largely diminished after coordinating transition metals in M-AAC, accompanied by an increase in O-C bond intensity (532. 3 eV) (Fig. S4) [29]. This trend supports a structural configuration in which metal oxides are anchored to the carbon surface through C-O-M linkages.

3.2. *Electrochemical properties of M-AAC*

The electro-sorption capacity of porous materials relies on their electrical capacitance, where charged species in the bulk solution are stored to counterbalance the polarity of the electrode surface. The voltammetric current density may arise from two concurrent charging/discharging processes: electrical double-layer (EDL) formation and electrode redox reactions. The EDL capacitance (C_{dl}) measures the surface charge (q, coulomb) at a given potential (E, volt), leading to an EDL current (I_{dl}) directly proportional to the scan rate (v, V s^{-1}):

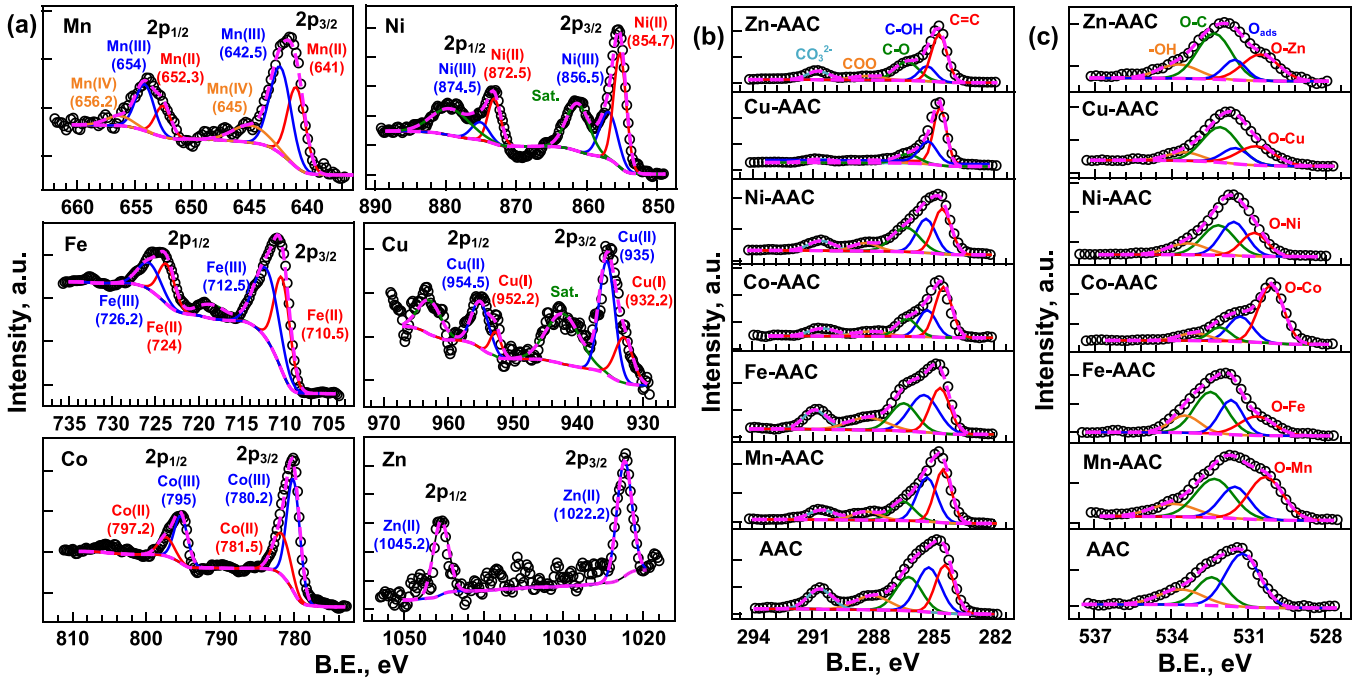

Fig. 3. XPS spectra at binding energies of (a) metal 2p, (b) C 1 s, and (c) O 1 s orbitals for M-AAC samples.

$C_{dl} = \frac{dq}{dE} = \frac{Idt}{dE} = \frac{I_{dl}}{v}$ [30]. On the other hand, according to Nernst theory, the Faradaic current from diffusion-controlled redox reactions (I_{diff}) can be evaluated as a function of $v^{1/2}$. Therefore, the total current density can be expressed as [31]:

$$I_{tot} = I_{dl} + I_{diff} = k_1 v + k_2 v^{1/2} \quad (1a)$$

and a linear form:

$$\frac{I}{v^{1/2}} = k_1 v^{1/2} + k_2 \quad (1b)$$

for scan rates ranging from 10 to 100 mV s^{-1} enables the extraction of EDL limiting constant k_1 and diffusive constant k_2. As demonstrated in Fig. 4a, the AAC electride exhibits a nearly symmetric voltammetry profile, excluding the oxygen evolution reaction (OER) beyond + 1.0 V (vs. RHE), with 27 % of I_{diff}, consistent with predominantly its EDL-driven nature. In contrast, the Co-AAC electrode in Fig. 4b displays distinct reversible peaks corresponding to metal oxide transformation (O_M/R_M), indicative of their pseudocapactivie behavior [32]. These Faradaic reactions, accounting for 51 % of the total current, suggest that metal oxide loading on carbon substrate introduces additional electro-active sites that enhance charge storage during anodic polarization. Fig. 4c compares the voltammetry of the Co-AAC electrode in 10 mM $NaHCO_3$, both in the absence and presence of 30 mM MoO_4^{2-}. The addition of Mo induces negligible changes in the characteristic redox couple (O_{Co}/R_{Co}), confirming that the Co^{II} to Co^{III} transition does not mediate electron transfer involving Mo species. In other words, during electro-sorption, molybdate oxidation or reduction insignificantly influence Mo removal.

Voltammetric measurements at various scan rates for all M-AAC electrodes are shown in Fig. S5, with the extracted DEL and diffusive capacitances summarized in Fig. 4d. The pristine AAC substrate presents the highest proportion of C_{dl}, while C_{diff} contributes to the majority of total capacitance in M-AAC electrodes. The largest three total capacitances are observed for Mn-AAC (94 mF cm^{-2}), Co-AAC (81 mF cm^{-2}), and Fe-AAC (68 mF cm^{-2}), far exceeding that of the unmodified AAC (14 mF cm^{-2}). Notably, this trend does not directly follow the s.s.a. order shown in Fig. 2j. Since the N_2 uptake method only measures the surface area associated with material porosity, it may misrepresent the ion-size effect on the number of active sites available for charge storage. Moreover, the diffusive capacitance depends on the magnitude of the Faradaic current, which primarily arises from the intercalated metal oxides. This discrepancy can be partially addressed by evaluating the electrochemical surface area (ECSA), typically estimated from the electrical capacitance [33]. Consequently, the specific surface area and pore size alone cannot fully explain the chemical affinity of metal oxides toward electrolyte ions, highlighting the importance of assessing ECSA in conjunction with textural properties. These findings also highlight that the pseudocapactance of M-AAC plays a dominant role in their electro-sorption capacity, in contrast to the EDL-driven mechanism observed in conventional CDI systems [34].

Fig. 4e displays the zeta-potential of M-AAC electrodes (10^{-1} M KCl) as a function of solution pH. The unmodified AAC sample exhibits the lowest pH of zero charge (pH_{pzc} = 2.2), which is attributed to surface acidity from carboxylic functional groups, resulting in a negatively charged surface at neutral pH. Upon incorporating various transition metals onto M-AAC, the pH_{pzc} shifts positively in the order: Co-AAC (7.8) > Cu-AAC ~ Zn-AAC ~ Ni-AAC (6) > Fe-AAC (5.5) > Mn-AAC (4.3). Such pH-reversible surface properties alter electrode polarity, likely affecting asymmetric adsorption toward anions and cations [35]. In addition, the transformation of metal oxide under applied potentials (i.e., pseudocapactance) introduces additional lattice charges [36,37]. Fig. 4f presents the charging/discharging cycles for Mo electro-sorption ($C_{Mo,0}$ = 10 mM) in the MCDI system at a constant potential (1.2 V). Co-AAC and Mn-AAC electrodes exhibit the highest steady-state currents. In chronoamperometry, the initial increase in current densities corresponds to electro-sorption when capacitive charging. The reversibility of Co_3O_4/CoOOH and MnOOH/MnO_2, well-documented in supercapacitor applications, contributes to the sustained current response [38]. The residual current density indicates that Mo adsorption is accompanied by reversible Faradaic processes.

Fig. 4g compares the electro-sorption performance of M-AAC through Ragone plots, which relate the specific adsorption capacity (SAC) to the specific adsorption rate (SAR, mg g^{-1} min^{-1}) [39]. Experiments were conducted at 1.0 V with an initial molybdate of 100 mg-Mo L^{-1}. Co-AAC demonstrates the fastest deionization rate, appearing in the uppermost right region of plot, indicative of both

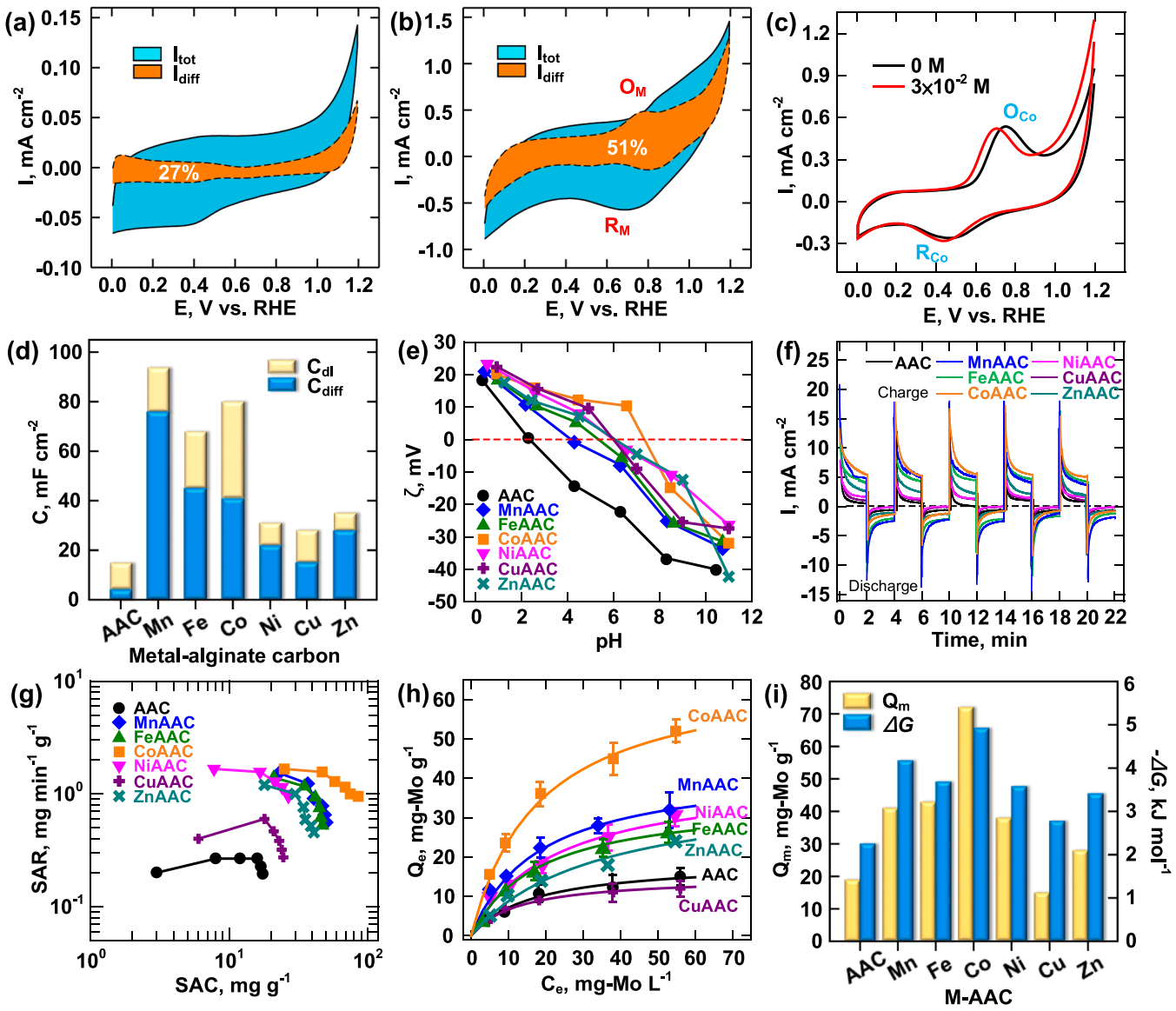

Fig. 4. Voltammetry of (a) AAC and (b) Co-AAC electrodes, with diffusive and total capacitive currents (10 mM $NaHCO_3$). (c) Voltammetry of Co-AAC without and with the addition of 30 mM MoO_4^{2-}. Effects of transition metal in M-AAC on (d) electrical capacitance and zeta-potential as a function of pH. (f) Chronoamperometry of charge/discharge cycles using M-AAC electrodes. (g) Regone plots for different M-AAC electrodes, and corresponding (h) adsorption isotherm, (i) monolayer capacity, and Gibbs free energy for molybdate anions.

capacity and rapid adsorption. The SAR followed the order: Co-AAC > Mn-AAC > Fe-AAC > Ni-AAC > Zn-AAC > Cu-AAC, with the unmodified AAC exhibiting the slowest electro-sorption rate. This trend aligns with the hypothesized influence of surface positivity among metal oxides, where Co-AAC possesses the highest pH_{pzc}, thereby favoring MoO_4^{2-} adsorption. The relatively high SAR values observed for Mn-AAC and Fe-AAC are attributed to their pseudocapacitive transformations, which generate additional positive charges at elevated potentials, despite their negatively charged surface functionalities at neutral pH. Furthermore, interactions between the electronic structures of metal oxides and molybdate may affect adsorption energy, and consequently SAR, as further elucidated by free energy calculations. Mo adsorption isotherms are obtained for each M-AAC to further evaluate their adsorption behavior under a constant potential of + 1.0 V (vs. RHE) (298 K, pH 6.5), as provided in Fig. 4h. The equilibrium capacity (Q_e, mg g^{-1}) after 90 min of adsorption was calculated using: $Q_e = \frac{C_0 - C_e}{m} \times V$ [40], where m is the mass (g) of the synthesized M-AAC material, C_e is the Mo concentration at 90 min, and C_0 is the initial Mo concentration (10 – 100 mg-Mo L^{-1}). Fitting the $Q_e - C_e$ relationship to the Langmuir model [41],

$$Q_e = \frac{K_L C_e Q_m}{1 + K_L C_e} \quad (2)$$

yielded the monolayer capacity (Q_m) and the equilibrium constant K_L (L mg^{-1}), from which the standard Gibbs free energies is calculated as $\Delta G^0_{ads} = -RT\ln K_L$. Q_m was determined from the intercept of the linear regression of C_e^{-1} versus Q_e^{-1}, as shown in Fig. S6, which provided a better fit for Mo adsorption compared to an empirical Freundlich model. As compared in Fig. 4i, the resulting monolayer capacity Q_m follow the sequence: Co-AAC (72 mg-Mo g^{-1}) > Fe-AAC (43 mg-Mo g^{-1}) > Mn-AAC (41 mg-Mo g^{-1}) > Ni-AAC (38 mg-Mo g^{-1}) > Zn-AAC (28 mg-Mo g^{-1}) > AAC (19 mg-Mo g^{-1}) > Cu-AAC (15 mg-Mo g^{-1}). Co-AAC obtains both the highest Q_m and ΔG^0_{ads} (-5.1 kJ mol^{-1}), verifying its relatively strong affinity for Mo, compared with unmodified AAC ($\Delta G^0_{ads} = -2.6$ kJ mol^{-1}). Properties of all M-AAC are summarized in Table S1.

Table 1 summarizes reported adsorptive treatments for molybdate

Table 1
Summary of adsorptive recovery for molybdate.

Material	Adsorbent	Condition	Capacity	Ref.
Iron oxide	αFeOOH	pH 4, 0.1 M NaCl	15.5 mg g^{-1}	[42]
	Fe_2O_3	pH5, 0.01 M $NaNO_3$	14.8 mg g^{-1}	[43]
	$SiO_2Fe_xO_y$	pH 8, $NaNO_3$	10.95 mg g^{-1}	[44]
	Fe_3O_4/Zeolite	pH3, 0.01 M $NaNO_3$	17.9 mg g^{-1}	[45]
	Fe-AAC (electrosorption, +1.0 V)	pH 6.5, 0.01 M $NaHCO_3$	43 mg g^{-1}	Present study
Manganese oxide	δMnO_2	pH4, 0.01 M $NaNO_3$	18.2 mg g^{-1}	[43]
	δMnO_2	pH 6, 0.001 M NaCl	5.65 mg g^{-1}	[46]
	Mn-AAC (electrosorption, +1.0 V)	pH 6.5, 0.01 M $NaHCO_3$	41 mg g^{-1}	Present study
Aluminum oxide	γAl_2O_3	pH 4, 0.03 $NaNO_3$	31 mg g^{-1}	[47]
	$NiAlZr(OH)_x$	pH 5	24.2 mg g^{-1}	[48]
Activated carbon	Coir pith carbon	pH 4	18.9 mg g^{-1}	[1]
	AAC (electrosorption, +1.0 V)	pH 6.5, 0.01 $NaHCO_3$	19 mg g^{-1}	Present study
Cobalt oxide	CoCRD (electrosorption, +1.0 V)	pH 6.5, 0.003 M $NaHCO_3$	87 mg g^{-1}	[24]
	Co-AAC (electrosorption, +1.0 V)	pH 6.5, 0.01 M $NaHCO_3$	72 mg g^{-1}	Present study

removal. Metal oxides are the most widely studied adsorbents and can be grouped into three major types: (1) iron oxide, such as goethite [42], ferrihydrite [43,44], and magnetite [45]; (2) manganese oxide, including δMnO_2 and birnessite [43,46]; (3) aluminum oxide, such as γAl_2O_3 and gibbsite [47,48], each exhibiting various distinct surface properties toward Mo adsorption, with capacities ranging in 10 – 40 mg-Mo g^{-1}. Biochar and activated carbon generally show lower capacities (below 20 mg-Mo g^{-1}) – similar to the present AAC electrode – due to their negatively charged surfaces [1]. Although transition metal oxides are widely utilized as pseudocapacitive materials in electrochemical systems [49–51], limited attention has been given to their application in the electro-sorption of specific ionic species. We previously demonstrated the first Mo recovery using Co-enriched carbon polyhedrons derived from metal-organic frameworks (MOFs) [24]. The redox transition of Co_3O_4 in the carbon framework was confirmed to enhance Mo uptake during anodization. This study adopted a more economical and straightforward route to integrate cobalt oxides into alginate-derived carbon, yielding a comparable capacity for Mo at neutral pH. Furthermore, the CDI system offers fast adsorption-desorption switching through polarity reversal, thereby increasing the capacities of Fe-AAC and Mn-AAC electrodes beyond those of Fe and Mn oxide adsorbents used in conventional adsorption processes.

Electro-sorption of molybdate on the AAC and Co-AAC surfaces under elevated potentials is investigated using operando Raman spectroscopy, as shown in Fig. 5a and Fig. 5b. Characteristic vibrational modes of the MoO_4^{2-} oxyanion at 321 and 846 cm^{-1} emerge upon applying working potential beyond + 0.6 V, confirming the accumulation of Mo species on electrode surfaces. At higher potentials, the intensified Raman band at 903 cm^{-1} corresponding to hepta-molybdate ion ($Mo_7O_{24}^{6-}$) indicates the condensation and complexation of adsorbed MoO_4^{2-} within the double-layer structure, even though MoO_4^{2-} remains predominantly as free ions in the dilute bulk solution at neutral pH [52]. Additionally, the Raman signals of Co_3O_4 – corresponding to the E_g (462 cm^{-1}), $F_{2\,g}$ (508/585 cm^{-1}), and $A_{1\,g}$ (677 cm^{1-}) modes – gradually diminished with increasing Mo loading. Meanwhile, elevated potentials strengthen the D and G bands of the carbon substrate, associated with structural disorder and graphitic domains in aromatic rings, respectively. These spectral evolutions reflect the redox activity of the pseudocapacitive material during Mo adsorption. The simulated electrostatic potential (ESP) distribution of the optimized MoO_4^{2-} geometry (Fig. 5c) predicts enhanced negative electron density around the four O atoms after deprotonation. Therefore, the Mo-O bonds are expected to orient toward the electrode surface under anodic polarization. In contrast, the isopoly-complex ion $Mo_7O_{24}^{6-}$ comprise seven MoO_6 octahedrons condensed by edge sharing, as shown in Fig. 5d, consistent with previous reports [6,53]. This optimized structure presents negative moieties that are doubly coordinated to active sites, as demonstrated by its ESP. Thus, at elevated anode potentials, the strengthened electrostatic attraction between the MoO_4^{2-} and exposed metal sites may promote the accumulation and formation of surface complexes under neutral pH conditions.

To further rationalize the variations in capacities across different M-AAC electrodes, DFT simulations were performed on optimized metal sites within carbon-metal (C-M), carbon-oxygen-metal (C-O-M), and metal oxide (O-M) configurations, as illustrated in Figs. 5e-5g. Detailed computational procedurals based on the $DMol^3$ modules are provided in the Supporting Information, where exposed metal oxide surfaces (Fig. S7) are established according to the XRD results. The tetrahedral molybdate is expected to form inner-sphere complexes [54], with one corner oxygen perpendicularly bound to the exposed metal atom in the carbon or oxygenated carbon framework. Fig. 5h summarizes the calculated free energies of MoO_4^{2-} adsorption on varied surfaces. Compared with the slightly positive energy (0.08 eV) on carbon (AAC), all M-AAC surfaces exhibit negative energies, indicating favorable adsorption. In mono-dentate configurations, the average M-O bond length between metal and molybdate oxygen is around 1.7 Å. In particular, Co-AAC shows the strongest affinity, with energies of −0.49 eV for C-Co and −0.82 eV for C-O-Co. Furthermore, for metal oxides, Co_3O_4 (0 0 1) presents the most preferred facet (-2.85 eV) for MoO_4^{2-} adsorption, followed by ZnO (0 0 1) (-2.59 eV). Fig. S8 presents the optimal geometries of MoO_4^{2-} on different oxides, with average M-O bond lengths of 1.9 Å. Depending on the atom distribution on the top layer of a slab, molybdate tends to form bidentate inner-sphere complexes on Co_3O_4 (0 0 1) and ZnO (0 0 1), adopting a pyramid orientation with a central ion bound to binuclear metal sites [55]. However, the strong affinity of ZnO for Mo species predicted by DFT was not translated into its experimental adsorption capacity. EDS analysis revealed that Zn-AAC contained a low metal content (<2 at%) due to Zn volatilization during carbonization, resulting in a limited number of active sites available for Mo uptake. On the other hand, under anodic polarization molybdate species condense on electrode surfaces to form hepta-molybdate, where two oxygen ligands of MoO_6 octahedra coordinate with metal sites, as revealed in Figs. 5i – 5l. The $Mo_7O_{24}^{6-}$ complex shows lower adsorption energies on C-O-M sites than MoO_4^{2-} ion. In optimal hepta-molybdate orientations, the adsorption strength increases with the number of Mo centers sharing bidentate oxygen ligands bound to Co sites, following: Co-2O-Mo (-2.28 eV) < Co-2O-2Mo (-2.37 eV) < Co-2O-3Mo (-2.56 eV) < Co-2O-4Mo (-3.65 eV). These simulation results indicate that Co-functionalized AAC electrodes provide the most favorable adsorption sites for both MoO_4^{2-} and condensed $Mo_7O_{24}^{6-}$ species. The strong inner-sphere and cooperative bidentate interactions explain the superior molybdate uptake observed electrochemically on Co-AAC compared to other M-AAC electrodes.

3.3. Electro-sorption of molybdate

The effect of working potential (0 to +1.6 V vs. RHE) on the electro-sorption and desorption of 10 mg-Mo L^{-1} molybdate anions is assessed using the Co-AAC electrode in MCDI cell, as illustrated in Fig. 6a. Mo removal efficiency markedly improves with potential up to + 0.8 V

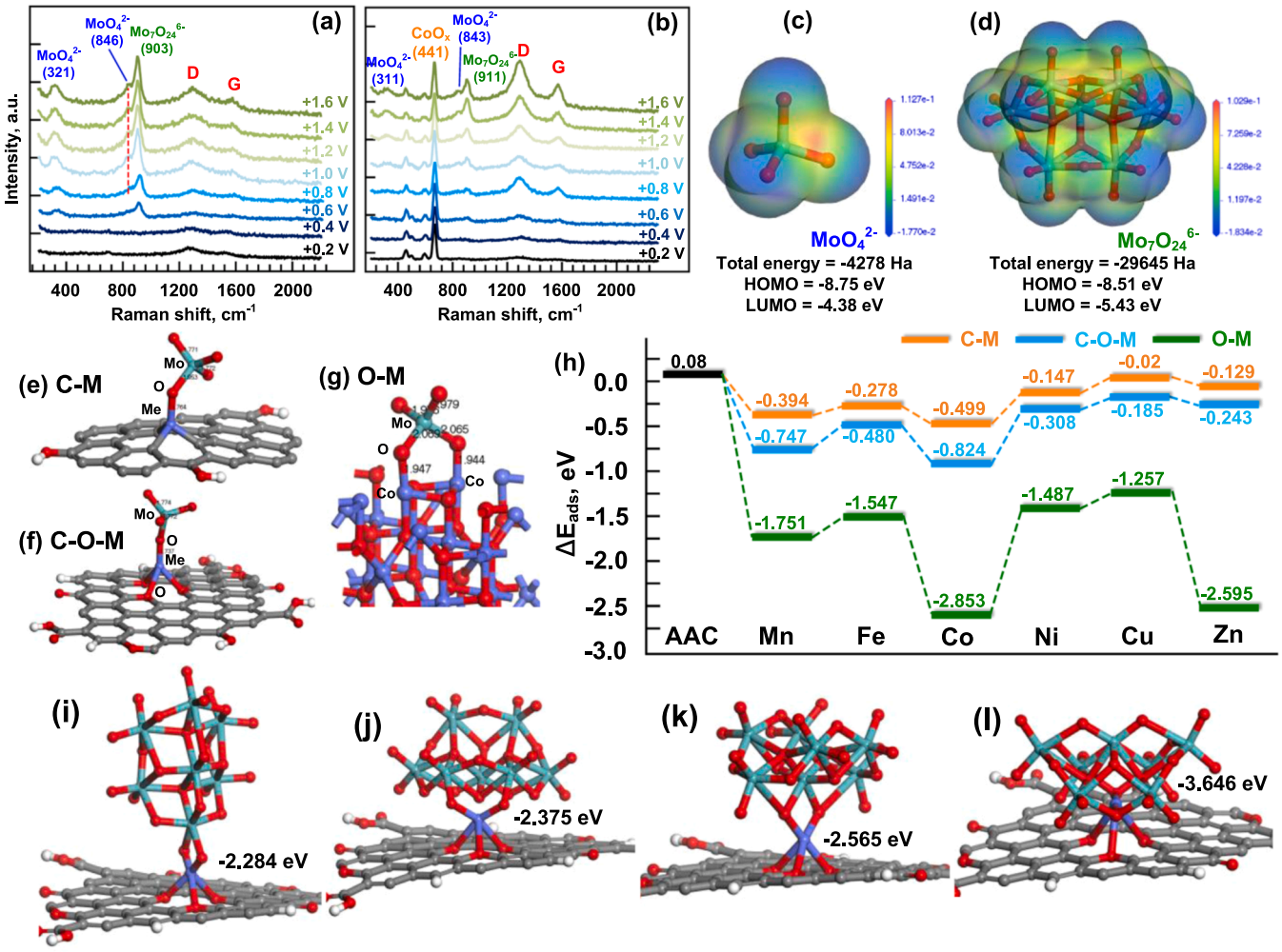

Fig. 5. Operando Raman spectroscopy of (a) AAC and (b) Co-AAC electrodes in the presence of 10 mM MoO_4^{2-} (10 mM $NaHCO_3$, pH 6.5). Electrostatic potential distribution (ESP) of (c) MoO_4^{2-} and (d) $Mo_7O_{24}^{6-}$. Optimal geometry of MoO_4^{2-} on surfaces of (e) carbon-metal, (f) carbon-oxygen-metal, and (g) metal oxide, with corresponding (h) adsorption energies for different M-AAC electrodes. Surface complexation of heptamolybdate ($Mo_7O_{24}^{6-}$) on C-O-M active sites in different bidentate orientations, (i) Co-2O-1Mo, (j) Co-2O-2Mo, (k) Co-2O-3Mo, and (l) Co-2O-4Mo.

(Fig. 4c), coinciding with the pseudocapacitive transformation of Co_3O_4 at the O_{Co} peak. In cobalt oxide capacitors, the surface charge arises from the redox transition of Co species [56,57]. During anodization, partial oxidation of Co^{2+} in $Co^{II}Co_2^{III}O_4$ to *CoOOH* generates additional surface positive charges (δ^+), which are compensated by the adsorption of anions (e.g., MoO_4^{2-}) to maintain charge neutrality.

$$Co^{II}Co_2^{III}O_4@C \rightleftharpoons Co_{1-\delta}^{II}Co_{2+\delta}^{III}O_4@C + \delta e^- \quad (O_{Co}/R_{Co}) \tag{3a}$$

$$(Co_3O_4)^{\delta+}@C + MoO_4^{2-} \rightleftharpoons (MoO_4^{2-})(Co_3O_4)^{\delta+}@C(\text{anion adsorption}) \tag{3b}$$

Although the Faradaic reaction does not directly involve electron transfer from adsorbed molybdate, MoO_4^{2-} or other electrolyte anions are trapped to balance these additional lattice charges during anodic polarization. As displayed in Fig. 6b, the monolayer capacity (Q_m) exceeds 70 mg-Mo g^{-1} at potentials > +1.2 V. However, the onset of side reactions, notably OER, at higher potentials may reduce the charge efficiency (CE, %) for Mo electro-sorption [58].

$$CE(\%) = \frac{2 \times F \times \Delta[MoO_4^{2-}] \times V}{\int Idt} \times 100 \tag{4}$$

Here, the time-integrated current, $\int Idt$, was obtained from chronoamperometry during charge-discharge cycles at various working potentials, as shown in Fig. S9. The term $\Delta[MoO_4^{2-}]$ represents the change in molar concentration of Mo during electrosorption, and F is the Faraday constant (96485 coulomb per mol). CE sharply declines to below 30 % at potentials > +1.2 V due to OER. Interestingly, CE values exceeding 100 % were observed at 0 – + 0.4 V, likely due to pH-reversible functional groups on Co-AAC. The surface hydrolysis, indicated by a positive zeta potential at pH below the pH_{pzc}, can promote Mo adsorption through electrostatic attraction. This non-faradaic process does not contribute to the charging current, leading to an overestimation of faradaic efficiency at low potentials.

To assess the effect of pH-reversible surfaces, Mo electro-sorption is conducted at pH ranging from 4 to 12, as shown in Fig. 6c. Mo removal efficiency is strongly dependent on the controlled pH, with the Co-AAC electrode exhibiting its maximal capacity at pH 6 – 8. The pH_{pzc} of Co-AAC was determined to be around 8 (Fig. 4e), indicating that its surface functional groups carry a positive charge at pH below this threshold [59]. This enhanced electrostatic attraction promotes migration current (I_{mig}), which potentially affects mass transport mechanism. On the other hand, molybdate speciation plays a critical role. Depending on pH and total Mo concentration, molybdate can associate with protons to form hepta-molybdate complexes according to [60]:

$$pMoO_4^{2-} + qH^+ \rightleftharpoons (MoO_4)_pH_q^{(2p-q)-}; \beta_{pq} \tag{5}$$

The formation constants β_{pq} are listed in Table S2. At pH below pK_{a1}

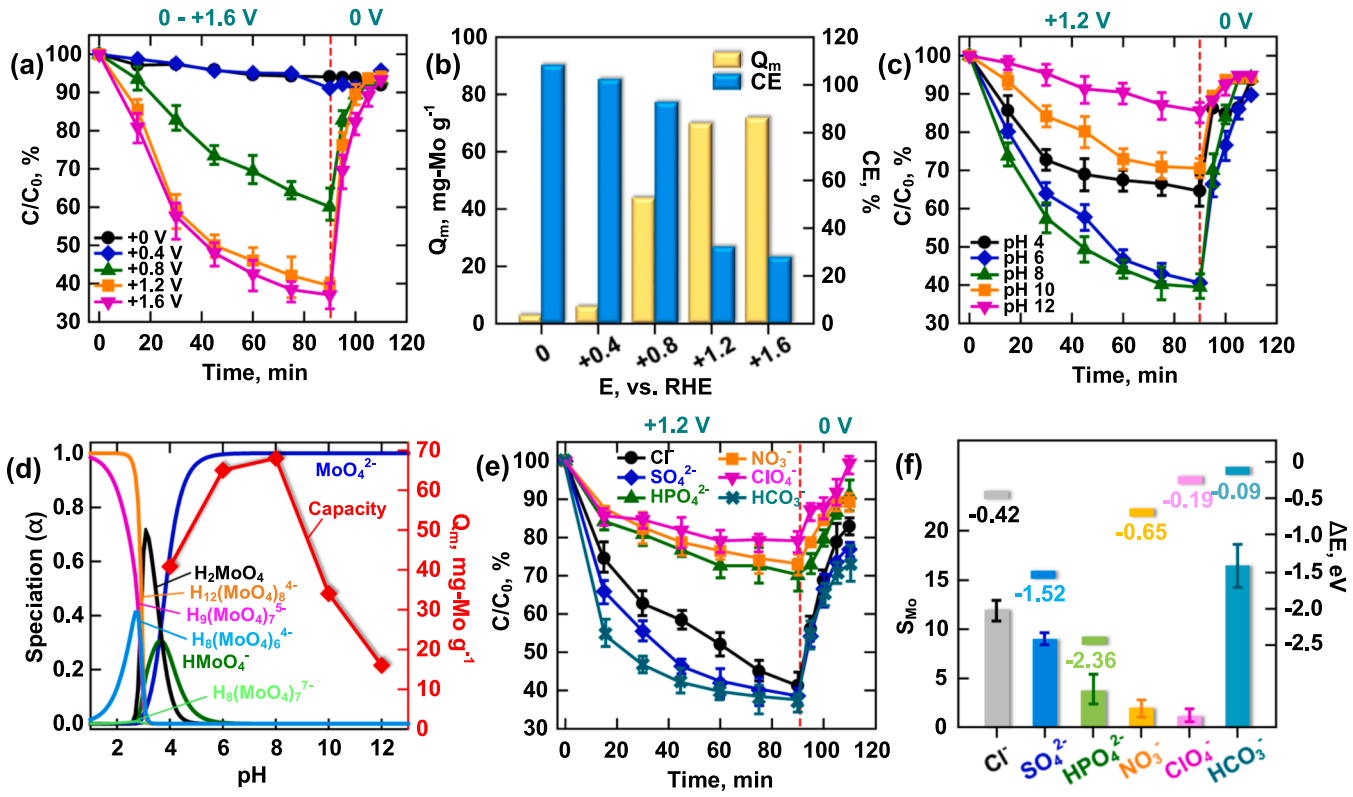

Fig. 6. Effects of working potential (vs. RHE) on (a) Mo electro-sorption/desorption (10 mg-Mo L^{-1}, 10 mM $NaHCO_3$), and (b) corresponding adsorption capacity (Q_m) and charge efficiency (CE). (c) Effect of solution pH and (d) Mo speciation on Mo removal and adsorption capacity. Effects of electrolyte type on (e) Mo electro-sorption/desorption and (f) selectivity factor and free energies of adsorption.

= 3.6, the uncharged diprotic H_2MoO_4 dominates, whereas at pH < 4 and total Mo concentration > 10^{-5} M, negatively charged oxyanions such as $H_8(MoO_4)_6^{4-}$, $H_8(MoO_4)_7^{7-}$, $H_9(MoO_4)_7^{5-}$, and $H_{12}(MoO_4)_8^{4-}$ become increasingly significant [61]. As shown in Fig. 6d, the variation of Q_m with pH closely follows the distribution of MoO_4^{2-} species, increasing pH from 4 to 8. For practical electro-sorption applications, CDI experiments were not conducted at pH below 4, even though such conditions could improve Mo removal through the formation of hepta-molybdate complexes.[7] At pH > 10, a sharp decline in Q_m values can be explained by the shift of surface function groups toward a negative charge, couple with side reactions such as water splitting [62,63].

As shown in Fig. 6e, various sodium salts (1 mM approximately tenfold the concentration of 10 mg-Mo L^{-1}) were introduced to assess the selectivity of Co-AAC for Mo electror-sorption. Under + 1.0 V (vs. RHE) and pH 6.5, the selectivity factor, $S_{Mo/x}$, was quantified according to [64]:

$$S_{Mo/x} = \left(\frac{C_{Mo,0} - C_{Mo,t}}{C_{x,0} - C_{x,t}}\right) \times \left(\frac{C_{x,0}}{C_{Mo,0}}\right) \quad (6)$$

where $C_{x,0}$ and $C_{x,t}$ are the initial and 90 min concentrations of the competing anion x, respectively. The resulting $S_{Mo/x}$ as summarized in Fig. 6f all exceed unity, reflecting the strong affinity of the Co-AAC electrode toward molybdate ions. Particularly, common surface-water ions such as bicarbonate (S_{Mo/HCO_3^-} = 17), sulfate ($S_{Mo/SO_4^{2-}}$ = 8.5), and chloride (S_{Mo/Cl^-} = 11.5) exhibit minimal interference. In contrast, HPO_4^{2-}, ClO_4^- and NO_3^- are markedly more competitive. Generally, adsorption favors multivalent ions over smaller, highly hydrated monovalent ions, with the strength of electrostatic interaction between ionic species and the surface charged center depending on both ionic valence and effective size [65]. The ratio of hydrated radius to crystal radius follows the order: HCO_3^- (1.97) > Cl^- (1.83) > SO_4^{2-} (1.39) > HPO_4^{2-} (1.27) > NO_3^- (1.26) > MoO_4^{2-} (1.19) > ClO_4^- (1.16), which inversely predicts the observed Mo selectivity. Additionally, DFT calculations revealed distinct adsorption energies of oxyanions on C–O–Co interfacial sites, as shown in Fig. S10. The optimized geometries indicate that phosphate (-2.36 eV) and sulfate (-1.53 eV) adsorb strongly in bidentate configurations, whereas nitrate (-0.65 eV) and carbonate (-0.08 eV) adopt weaker monodentate adsorption. Perchlorate (-0.19 eV) and chloride (-0.42 eV) tends to form weak outer-sphere complexes with oxide surfaces owing to its diffuse hydration shell. This adsorption energy sequence rationalizes the preferential uptake of molybdate (-1.36 eV) over coexisting oxyanions on Co–AAC. However, the relatively low selectivity of molybdate against perchlorate and nitrate can be attributed to their higher diffusivity within the carbon pores [65], a factor not fully captured by electronic structure simulations.

To validate the CDI application for Mo recovery, electro-sorption experiments were conducted using various real-water samples, including groundwater (GW), wastewater treatment plant effluent (WWT), and two river waters. The compositions of these waters are summarized in Table S3. As illustrated in Fig. 7a, Mo removal in GW and WWT shows negligible deviation from that in the blank electrolyte (i.e., 10 mM $NaHCO_3$), indicating minimal matrix interference. In contrast, both two river samples significantly reduce the Mo adsorption capacity to 30 % that in the blank, which can be attributed to their extremely high salinity. The corresponding ionic strengths were determined as 0.026, 0.018, 0.77, and 0.66 eq L^{-1} for GW, WWT, and two river waters, respectively. The river water can be categorized as brackish, where the elevated chloride concentrations strongly compete with Mo species for the active sites on the Co-AAC electrode. It is noted that Mo was not completely released during the desorption stage, likely due to competitive adsorption among coexisting complex ions. Additionally, the formation of insoluble metal molybdates may contribute to Mo removal; however, this effect is considered negligible given the low initial Mo concentration of 10 mg L^{-1}. The cycling performance of the Co-AAC electrode is assessed in Fig. 7b. Each cycle of the repeated electro-

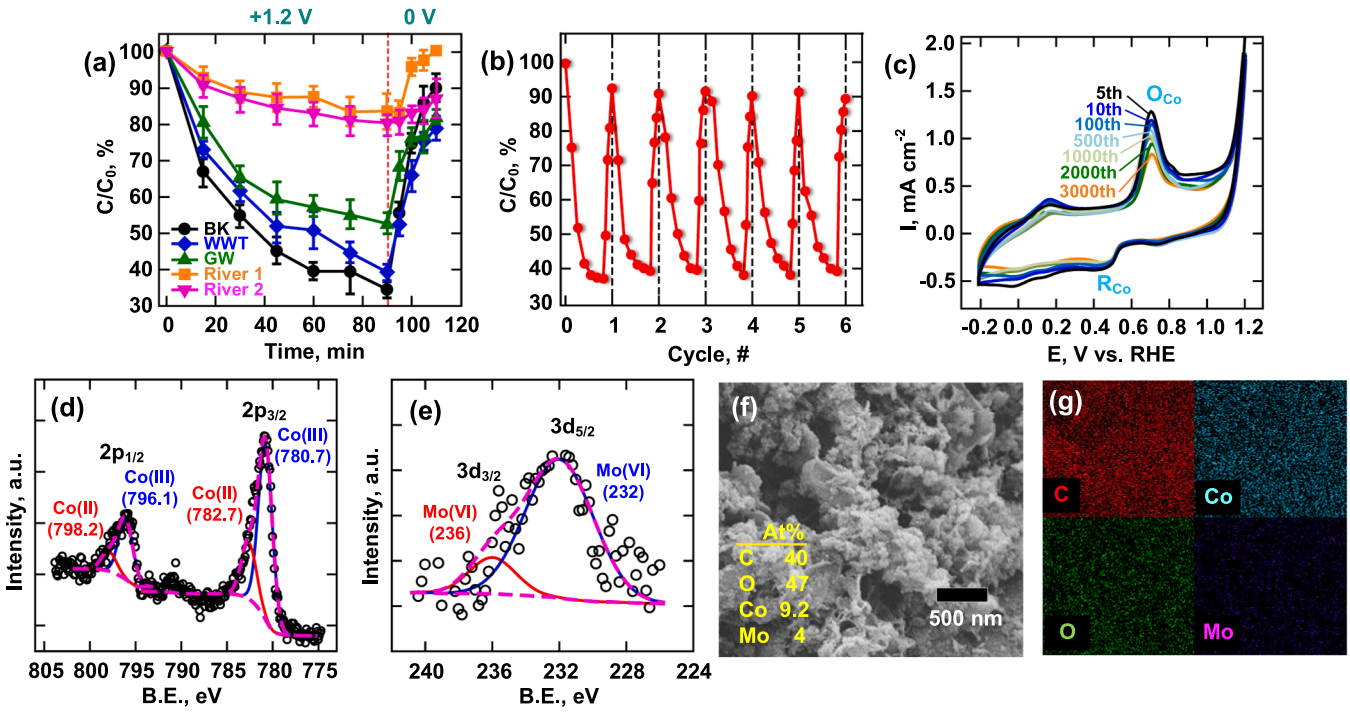

Fig. 7. (a) Electro-sorption of Co-AAC electrode in different real water samples (10 mg-Mo L^{-1}), (b) cycling performance for Mo removal, where each cycle consisted of electro-sorption at + 1.0 V for 90 min and desorption at 0 V for 20 min. (c) Repeating voltammetry scans of the Co-AAC electrode (electrolyte = 10 mM $NaHCO_3$). XPS at (d) Co 2p and (e) Mo 3d binding energies, (f) SEM image, and (g) elemental mappings of Co-AAC electrode after Mo electro-sorption cycles.

sorption and desorption consisted of a 90-min phase at + 1.0 V, followed by 20-min phase at 0 V in a 10 mg-Mo L^{-1} solution. The electrode achieves a Mo removal efficiency of over 60 % during the first cycle, and maintains at least 50 % over the subsequent five cycles. Although desorption was incomplete (~90 %) in each cycle, this limitation did not significantly affect electrode stability, demonstrating effective Mo recyclability through simple potential switching. A low activation energy (1.38 kJ mol^{-1}), derived from the rate constants of Mo removal at different electrolytic temperatures (Fig. S11), confirms the physical adsorption nature of Mo on Co-AAC. The reduction in the energy barrier may also be rationalized by the enhanced surface wettability resulting from Co incorporation into the Co-AAC electrode, as evidenced by the decreased contact angles shown in Fig. S12 (66.4°, compared to 97.7° for AAC). On the other hand, the electrical energy per order (*EE/O*), specifically required to reduce the Mo concentration by one order of magnitude, was calculated using the following equation:

$$EE\Big/O\left(Whg^{-1}\right)=\frac{E\times I\times t_{90}}{m}=\frac{2.302E\times I}{m\times k_{obs}} \tag{7}$$

where E and I are the applied potential and current, t_{90} is the time to achieve 90 % removal, which can be expressed as $2.302/k_{obs}$ based on the observed rate constant (k_{obs}, h^{-1}), and *m* is the mass of Mo removed. During electro-sorption cycles, the average EE/O are 9.1 Wh g(Mo)$^{-1}$, comparable to that of conventional CDI for desalination (3 – 6 Wh g $(NaCl)^{-1}$, depending on salinity) [66].

The electrode durability is further examined by extending cyclic voltammetry in Mo solution, as displayed in Fig. 7c. The Co redox peaks remain stable during the first 100 scans but gradually decrease between 100 – 3000 scans, indicating partial surface passivation or restructuring of Co sites. Nevertheless, the persistence of O_{Co} peak current throughout these scans confirms the long-term stability via the electrode's pseudocapacitive mechanism. Figs. 7d and 7e present the chemical state evolution of Co 2p and Mo 3d in the used CoAAC electrode after cycling Mo electro-sorption experiments. Compared to the fresh electrode (Fig. 3a), the Co^{3+} fraction at 780.7 eV ($2p_{3/2}$ orbital) increases from 66 % to 74 %, suggesting partial passivation during operation. Since the Mo electro-sorption involves repeated charge/discharge phases, the reversible shift in Co oxidation state confirms the participation of the Co_3O_4 to CoOOH redox reactions. Concurrently, the appearance of Mo (VI) $3d_{5/2}$ and $3d_{3/2}$ peaks at 232.5 and 236 eV, respectively, evidences Mo residues, primarily as molybdate (VI) species [67]. Complementary SEM image and elemental mappings (Figs. 7f and 7g) reveal that Mo accounts for around 4 % after electro-sorption/desorption cycles. The simultaneous enrichment of O and Mo signals indicates surface reconstruction during Co^{2+}/Co^{3+} transition, which promotes stable binding and release of Mo species.

4. Conclusions

Molybdate pollutants in industrial effluents pose ecological and human health risks but also represent a valuable resource. To enhance Mo recovery from water, a MCDI method with rapid adsorption/desorption via potential reversal was employed. Metal oxide-carbon composites, M-AAC, were synthesized from alginate and transition metal precursors for Mo electro-sorption. The mesoporous carbon framework endowed the metal oxides with pseudocapacitive charge storage under anodic polarization, while alginate-activated carbon promoted uniform metal dispersion, thereby improving electrode's adsorption capacity. Among electrodes, Co-AAC demonstrated the highest adsorption capacity for Mo. DFT simulations suggested preferential binding of Mo – in forms of MoO_4^{2-} or $Mo_7O_{24}^{6-}$ – on Co active sites, including C-Co, C-O-Co, and Co_3O_4. Although characterization revealed an increased oxidation state of Co oxide resulting from moderate passivation during repeated charge–discharge cycles, its capacity for Mo electro-sorption showed negligible decay. Moreover, the MCDI system maintained stable performance in the presence of various competing anions and in complex water matrices, including municipal wastewater, groundwater, and river water. This study highlights alginate-based CDI electrodes as a promising platform for Mo recovery.

Environmental implication

Molybdenum-containing waste is primarily generated from industrial processes. Elevated Mo concentrations in environments can exert harmful effects on human health. Electro-sorption has emerged as an economical method for recovering the valuable Mo resource, simply via polarity reversal. An alginate-derived carbon confined with transition metals were synthesized to enhance the adsorption capacity, where interactions between molybdate and metal oxides were hypothetically assessed. To optimize electrode performance, electrosorption-desorption experiments were validated in various water matrices.

CRediT authorship contribution statement

Zhi-Lun Wu: Software, Methodology, Investigation, Formal analysis. **Chi-Yun Shen:** Writing – original draft, Methodology, Investigation, Formal analysis, Data curation. **Chin-Pao Huang:** Conceptualization, Investigation, Methodology, Validation. **Yu-Jen Shih:** Writing – review & editing, Writing – original draft, Visualization, Validation, Supervision, Resources, Project administration, Funding acquisition, Data curation, Conceptualization.

Declaration of Competing Interest

The authors declare that they have no known competing financial interests or personal relationships that could have appeared to influence the work reported in this paper.

Acknowledgement

The National Science and Technology Council, Taiwan, is appreciated for generous finance support of this research project under Contract No. NSTC 114–2221-E-110–005-MY3.

Appendix A. Supporting information

Supplementary data associated with this article can be found in the online version at doi:10.1016/j.jhazmat.2025.140623.

Data availability

Data will be made available on request.

References

[1] Namasivayam, C., Sangeetha, D., 2006. Removal of molybdate from water by adsorption onto $ZnCl_2$ activated coir pith carbon. Biores Technol 97 (10), 1194–1200. https://doi.org/10.1016/j.biortech.2005.05.008.

[2] Abejón, R., 2022. An overview to technical solutions for molybdenum removal: perspective from the analysis of the scientific literature on molybdenum and drinking water (1990–2019). Water 14 (13), 2108. https://doi.org/10.3390/w14132108.

[3] Pichler, T., Koopmann, S., 2020. Should monitoring of molybdenum (Mo) in groundwater, drinking water and well permitting made mandatory? Environ Sci Technol 54, 1–2. https://doi.org/10.1021/acs.est.9b06869.

[4] Kumar, R., Liu, C., Ha, G.S., Kim, K.H., Chakrabortty, S., Tripathy, S.K., Park, Y.K., Khan, M.A., Yadav, K.K., Cabral-Pinto, M.M.S., Jeon, B.H., 2023. A novel membrane-integrated sustainable technology for downstream recovery of molybdenum from industrial wastewater. Res Cons Recycl 196, 107035. https://doi.org/10.1016/j.resconrec.2023.107035.

[5] Yang, P.T., Wang, S.L., 2021. Sorption and speciation of molybdate in soils: implications for molybdenum mobility and availability. J Hazard Mater 408, 124934. https://doi.org/10.1016/j.jhazmat.2020.124934.

[6] Evans, H.T., Gatehouse, B.M., Leverett, P., 1975. Crystal structure of the heptamolybdate(VI) (paramolybdate) ion, $[Mo_7O_{24}]^{6-}$, in the ammonium and potassium tetrahydrate salts. J Chem Soc Dalton Trans 505–514. https://doi.org/10.1039/DT9750000505.

[7] Bourikas, K., Hiemstra, T., Van Riemsdijk, W.H., 2001. Adsorption of molybdate monomers and polymers on titania with a multisite approach. J Phys Chem B 105 (12), 2393–2403. https://doi.org/10.1021/jp002267q.

[8] Shin, Y.U., Yu, S.I., Jeon, J., Kim, H., Kim, T., Cheng, L.H., Bae, H., Jang, A., 2025. Exploring critical pathways using robust strategies: nanodiamond electrocatalysts for promoting boron removal via electrosorption. Water Res 273, 123080. https://doi.org/10.1016/j.watres.2024.123080.

[9] Nordstrand, J., Toledo-Carrillo, E., Dutta, J., 2023. Tuning the cation/anion adsorption balance with a multi-electrode capacitive-deionization process. J Electrochem Soc 170, 023502. https://doi.org/10.1149/1945-7111/acb84c.

[10] Ahirrao, D.J., Jha, N., 2019. Comparative study on the electrosorption properties of carbon fabric, functionalized multiwall carbon nanotubes and solar-reduced graphene oxide for flow through electrode based desalination studies. Carbon 152, 837–850. https://doi.org/10.1016/j.carbon.2019.06.078.

[11] Omosebi, A., Gao, X., Landon, J., Liu, K., 2014. Asymmetric Electrode Configuration for Enhanced Membrane Capacitive Deionization. ACS Appl Mater Interfaces 6 (15), 12640–12649. https://doi.org/10.1021/am5026209.

[12] Sharker, T., Gamaethiralalage, J.G., Qu, Q., Xiao, X., Dykstra, J.E., de Smet, L.C.P. M., Muff, J., 2024. Iron-loaded activated carbon cloth as CDI electrode material for selective recovery of phosphate. Environ Sci Pollut Res 31, 63734–63746. https://doi.org/10.1007/s11356-024-35444-7.

[13] Yin, H., Huang, L., Dai, Y., Zheng, Z., Li, Y., Tang, B., Wang, X., Shi, L., 2025. In-situ redox processes of electrosorption-based systems during As, Cr detoxification and recovery: mechanisms, applications and challenges. Chem Eng J 503, 157946. https://doi.org/10.1016/j.cej.2024.157946.

[14] Sassi, W., Boubaker, H., Ben-khaled, H., Dhaoui, S., Ghorbal, A., Hihn, J.Y., 2021. Modelization and implementation of free adsorption and electrosorption of Cr (VI) from wastewater using Al2O3 nanoparticles: assessment and comparison of the two processes. Environ Sci Pollut Res 28, 28349–28366. https://doi.org/10.1007/s11356-021-12612-7.

[15] Chen, J., Yun, S., Shi, J., Wang, Z., Abbas, Y., Wang, K., Han, F., Jia, B., Xu, H., Xing, T., Li, B., 2020. Role of biomass-derived carbon-based composite accelerants in enhanced anaerobic digestion: Focusing on biogas yield, fertilizer utilization, and density functional theory calculations. Biore Technol 307, 123204. https://doi.org/10.1016/j.biortech.2020.123204.

[16] Tang, K., Hong, T.Z.X., You, L., Zhou, K., 2019. Carbon–metal compound composite electrodes for capacitive deionization: synthesis, development and applications. J Mater Chem A 7, 26693–26743. https://doi.org/10.1039/C9TA08663C.

[17] Wang, X., Yun, S., Fang, W., Zhang, C., Liang, X., Lei, Z., Liu, Z., 2018. Layer-Stacking Activated Carbon Derived from Sunflower Stalk as Electrode Materials for High-Performance Supercapacitors. ACS Sust Chem Eng 6, 11397–11407. https://doi.org/10.1021/acssuschemeng.8b01334.

[18] Wang, Z., Yun, S., Wang, X., Wang, C., Si, Y., Zhang, Y., Xu, H., 2019. Aloe peel-derived honeycomb-like bio-based carbon with controllable morphology and its superior electrochemical properties for new energy devices. Ceram Intern 45, 4208–4218. https://doi.org/10.1016/j.ceramint.2018.11.091.

[19] Garland, N., Gordon, R., Hopkins, I., Ward, E., McElroy, C.R., MacQuarrie, D., Parkin, l, 2025. Polysaccharide-derived sulfur-containing mesoporous carbon materials for platinum group metal recovery. Carbon 239, 120309. https://doi.org/10.1016/j.carbon.2025.120309.

[20] Roquero, D.M., Othman, A., Melman, A., Katz, E., 2022. Iron(iii)-cross-linked alginate hydrogels: a critical review. Mater Adv 3, 1849–1873. https://doi.org/10.1039/d1ma00959a.

[21] Kumar, A., Das, T., Thakur, R.S., Fatima, Z., Prasad, S., Ansari, N.G., Patel, D.K., 2022. Synthesis of Biomass-Derived Activated Carbons and Their Immobilization on Alginate Gels for the Simultaneous Removal of Cr(VI), Cd(II), Pb(II), As(III), and Hg(II) from Water. ACS Omega 7, 41997–42011. https://doi.org/10.1021/acsomega.2c03786.

[22] Hassan, A.F., Abdel-Mohsen, A.M., Fouda, M.M.G., 2014. Comparative study of calcium alginate, activated carbon, and their composite beads on methylene blue adsorption. Carbohyd Pol 102, 192–198. https://doi.org/10.1016/j.carbpol.2013.10.104.

[23] Park, H.G., Kim, T.W., Chae, M.Y., Yoo, I.K., 2007. Activated carbon-containing alginate adsorbent for the simultaneous removal of heavy metals and toxic organics. Proc Biochem 42, 1371–1377. https://doi.org/10.1016/j.procbio.2007.06.016.

[24] Shih, Y.J., Wu, Z.L., Wang, M.R., Huang, C.P., 2025. Catalytic phase transition of cobalt oxide enriched in mesoporous carbon polyhedrons for electrosorption of molybdate oxyanions. Chem Eng J 518, 164426. https://doi.org/10.1016/j.cej.2025.164426.

[25] Hassanvand, A., Chen, G.Q., Webley, P.A., Kentish, S.E., 2018. A comparison of multicomponent electrosorption in capacitive deionization and membrane capacitive deionization. Water Res 131, 100–109. https://doi.org/10.1016/j.watres.2017.12.015.

[26] Bläker, C., Muthmann, J., Pasel, C., Bathen, D., 2019. Characterization of activated carbon adsorbents – state of the art and novel approaches. ChemBioEng Rev 6, 119–138. https://doi.org/10.1002/cben.201900008.

[27] Sangon, S., Kotebantao, K., Suyala, T., Ngernyen, Y., Hunt, A.J., Supanchaiyamat, N., 2024. $ZnCl_2$ activated mesoporous carbon from rice straw: optimization of its synthetic process and its application as a highly efficient adsorbent for amoxicillin. Environ Sci Water Res Technol 10, 1389–1405. https://doi.org/10.1039/D4EW00171K.

[28] Smith, M., Scudiero, L., Espinal, J., McEwen, J.S., Garcia-Perez, M., 2016. Improving the deconvolution and interpretation of XPS spectra from chars by ab initio calculations. Carbon 110, 155–171. https://doi.org/10.1016/j.carbon.2016.09.012.

[29] Idriss, H., 2021. On the wrong assignment of the XPS O1s signal at 531–532 eV attributed to oxygen vacancies in photo- and electro-catalysts for water splitting and other materials applications. Surf Sci 712, 121894. https://doi.org/10.1016/j.susc.2021.121894.

[30] Suryanto, B.H.R., Chen, S., Duan, O., Zhao, C., 2016. Hydrothermally driven transformation of oxygen functional groups at multiwall carbon nanotubes for improved electrocatalytic applications. ACS Appl Mater Inter 8, 35513–35522. https://doi.org/10.1021/acsami.6b14090.
[31] Pandey, P., Bhowmick, S., Qureshi, M., 2023. Magnetically triggered interplay of capacitive and diffusion contributions for boosted supercapacitor performance. ACS Appl Mater Inter 15, 39435–39447. https://doi.org/10.1021/acsami.3c08988.
[32] George, J., Balachandran, M., 2023. Extrinsic pseudocapacitance: tapering the borderline between pseudocapacitive and battery type electrode materials for energy storage applications. J Energ Storag 74, 109292. https://doi.org/10.1016/j.est.2023.109292.
[33] Roy, A., Ray, A., Saha, S., Ghosh, M., Das, T., Nandi, M., Lal, G., Das, S., 2021. Influence of electrochemical active surface area on the oxygen evolution reaction and energy storage performance of MnO2-multiwalled carbon nanotube composite. Int J Energy Res 45 (11), 16908–16921. https://doi.org/10.1002/er.6885.
[34] Aderyani, S., Flouda, P., Shah, S.A., Green, M.J., Lutkenhaus, J.L., Ardebili, H., 2021. Simulation of cyclic voltammetry in structural supercapacitors with pseudocapacitance behavior. Electrochim Acta 390, 138822. https://doi.org/10.1016/j.electacta.2021.138822.
[35] Lado, J.J., Pérez-Roa, R.E., Wouters, J.J., Isabel, M., Tejedor, T., Federspill, C., Anderson, M.A., 2015. Continuous cycling of an asymmetric capacitive deionization system: an evaluation of the electrode performance and stability. J Environ Chem Eng 3, 2358–2367. https://doi.org/10.1016/j.jece.2015.08.025.
[36] Huang, J., Clark, A.H., Hales, N., Crossley, K., Guehl, J., Skoupy, R., Schmidt, T.J., Fabbri, E., 2025. Oxidation of interfacial cobalt controls the pH dependence of the oxygen evolution reaction. Nat Chem 17, 856–864. https://doi.org/10.1038/s41557-025-01784-1.
[37] Chiu, Y.H., Cheshideh, H., Jagtap, A.A., Chung, R.J., Lin, L.Y., 2025. Breaking charge transport barriers with synergistic redox dynamics in cobalt tellurium oxide-modified $BiVO_4$: experimental and DFT insights into enhanced photoelectrochemical water oxidation. Chem Eng J 521, 166650. https://doi.org/10.1016/j.cej.2025.166650.
[38] Lin, C.K., Lin, P.C., Shih, S.J., Chang, C.J., Shi, J.B., Chen, C.Y., 2017. Pseudocapacitive performance of manganese oxide coated hierarchical cobalt oxide structure prepared by hydrothermal process. Ceram Intern 43, S739–S746. https://doi.org/10.1016/j.ceramint.2017.05.288.
[39] Kim, T., Yoon, J., 2015. CDI ragone plot as a functional tool to evaluate desalination performance in capacitive deionization. RSC Adv 5, 1456–1461. https://doi.org/10.1039/C4RA11257A.
[40] Datar, S.D., Mohanapriya, K., Ahirrao, D.J., Jha, N., 2021. Comparative study of electrosorption performance of solar reduced graphene oxide in flow-between and flow-through capacitive deionization architectures. Sep Purif Technol 257, 117972. https://doi.org/10.1016/j.seppur.2020.117972.
[41] Ahirrao, D.J., Tambat, S., Pandit, A.B., Jha, N., 2019. Sweet-lime-peels-derived activated-carbon-based electrode for highly efficient supercapacitor and flow-through water desalination. Chem Sel 4 (9), 2610–2625. https://doi.org/10.1002/slct.201803417.
[42] Xu, N., Christodoulatos, C., Braida, W., 2006. Modeling the competitive effect of phosphate, sulfate, silicate, and tungstate anions on the adsorption of molybdate onto goethite. Chemosphere 64, 1325–1333. https://doi.org/10.1016/j.chemosphere.2005.12.043.
[43] Kashiwabara, T., Takahashi, Y., Tanimizu, M., Usui, A., 2011. Molecular-scale mechanisms of distribution and isotopic fractionation of molybdenum between seawater and ferromanganese oxides. Geochim Cosmochim Acta 75, 5762–5784. https://doi.org/10.1016/j.gca.2011.07.022.
[44] Matusoiu, F., Negrea, A., Ciopec, M., Duteanu, N., Negrea, P., Svera, P., Ianasi, C., 2022. Molybdate recovery by adsorption onto silica matrix and iron oxide based composites. Gels 8, 125. https://doi.org/10.3390/gels8020125.
[45] Verbinnen, B., Block, C., Hannes, D., Lievens, P., Vaclavikova, M., Stefusova, K., Gallios, G., Vandecasteele, C., 2012. Removal of molybdate anions from water by adsorption on zeolite-supported magnetite. Water Environ Res 84, 753–760. https://doi.org/10.2175/106143012X13373550427318.
[46] Cui, M., Luther III, G.W., Gomes, M., 2021. Cycling of W and Mo species in natural sulfidic waters and their sorption mechanisms on MnO_2 and implications for paired W and Mo records as a redox proxy. Geochim Cosmochim Acta 295, 24–48. https://doi.org/10.1016/j.gca.2020.12.007.
[47] Kurmysheva, Y.A., Vedenyapina, M.D., Kulaishin, S.A., Podrabinnik, P., Pinargote, N.W.S., Smirnov, A., Metel, A.S., Bartolomé, J.F., Grigoriev, S.N., 2023. Adsorption removal of Mo(VI) from an aqueous solution by alumina with the subsequent regeneration of the adsorbent. Int J Mol Sci 24, 8700. https://doi.org/10.3390/ijms24108700.
[48] Ogata, F., Kurazaki, M., Nagai, N., Uematsu, Y., Toda, M., Otani, M., Saenjum, C., Taneie, S., Kawasaki, N., 2025. Recovery of molybdenum using adsorption/desorption by nickel–aluminum or nickel–aluminum–zirconium complex hydroxides from aqueous media. RSC Adv 15, 24475–24482. https://doi.org/10.1039/D5RA02921J.
[49] Javed, M.S., Khan, A.J., Hanif, M., Nazir, M.T., Hussain, S., Saleem, M., Raza, R., Yun, S., Liu, Z., 2021. Engineering the performance of negative electrode for supercapacitor by polyaniline coated Fe3O4 nanoparticles enables high stability up to 25,000 cycles. Intern J Hydrog Energ 46, 9976–9987. https://doi.org/10.1016/j.ijhydene.2020.04.173.
[50] Gao, Z., Yun, S., Yang, C., Zhang, Y., Dang, J., Yang, G., Yang, T., Qiao, D., Wang, K., 2023. Niobium- and cobalt-modified dual-source-derived porous carbon with a honeycomb-like stable structure for supercapacitor and hydrogen evolution reaction. J Colloid Interf Sci 639, 33–48. https://doi.org/10.1016/j.jcis.2023.02.032.
[51] Xu, Y., Chen, B., jiang, T., Zhou, H., 2025. Rational in-situ construction of oxygen-deficient and carbon-coated TiO2 hollow nanotubes for high-performance electrochemical desalination. Chem Eng J 521, 166487. https://doi.org/10.1016/j.cej.2025.166487.
[52] Payen, E., Grimblot, J., Kasztelan, S., 1987. Study of oxidic and reduced alumina-supported molybdate and heptamolybdate species by in situ laser Raman spectroscopy. J Phys Chem 91, 6642–6648. https://doi.org/10.1021/j100311a018.
[53] Marianski, M., Seo, J., Mucha, E., Thomas, D.A., Jung, S., Schlögl, R., Meijer, G., Trunschke, A., von Helden, G., 2019. Structural characterization of molybdenum oxide nanoclusters using ion mobility spectrometry–mass spectrometry and infrared action spectroscopy. J Phys Chem C 123 (13), 7845–7853. https://doi.org/10.1021/acs.jpcc.8b06985.
[54] Wang, S., Zeng, X., Lin, J., Yuan, Z., Qu, S., Zhang, B., Pan, Y., Chen, N., Chen, W., Jia, Y., 2021. Molecular structure of molybdate adsorption on goethite at pH 5–8: A combined DFT + U, EXAFS, and ab initio XANES study (C). J Phys Chem 125 (40), 22052–22063. https://doi.org/10.1021/acs.jpcc.1c05497.
[55] Zhang, J., Coker, V.S., Mosselmans, J.F.W., Shaw, S., 2022. Adsorption of octahedral mono-molybdate and poly-molybdate onto hematite: a multi-technique approach. J Hazard Mater 431, 128564. https://doi.org/10.1016/j.jhazmat.2022.128564.
[56] Jayakumar, M., Hemalatha, K., Chander, A.A., Sahu, A.K., Prakash, A.S., 2017. Origin of charge storage in cobalt oxide - Anchored graphene nanocomposites. Carbon 125, 168–179. https://doi.org/10.1016/j.carbon.2017.09.002.
[57] Zallouz, S., Réty, B., Vidal, L., Meins, J.M., Le, C.M., Ghimbeu, 2021. Co_3O_4 nanoparticles embedded in mesoporous carbon for supercapacitor applications. ACS Appl Nano Mater 4 (5), 5022–5037. https://doi.org/10.1021/acsanm.1c00522.
[58] Mossad, M., Zou, L., 2013. Evaluation of the salt removal efficiency of capacitive deionisation: Kinetics, isotherms and thermodynamics. Chem Eng J 223, 704–713. https://doi.org/10.1016/j.cej.2013.03.058.
[59] Choi, J., Lee, H., Hong, S., 2016. Capacitive deionization (CDI) integrated with monovalent cation selective membrane for producing divalent cation-rich solution. Desalination 400, 38–46. https://doi.org/10.1016/j.desal.2016.09.016.
[60] Cruywagen, J.J., Draaijer, A.G., Heyns, J.B.B., Rohwer, E.A., 2002. Molybdenum (VI) equilibria in different ionic media. Formation constants and thermodynamic quantities. Inorg Chim Acta 331, 322–329. https://doi.org/10.1016/S0020-1693(02)00700-4.
[61] Vissenberg, M.J., Joosten, L.J.M., Heffels, M.M.E.H., van Welsenes, A.J., de Beer, V.H.J., van Santen, R.A., van Veen, J.A.R., 2000. Tungstate versus molybdate adsorption on oxidic surfaces: a chemical approach. J Phys Chem B 104 (35), 8456–8461. https://doi.org/10.1021/jp993754c.
[62] Arulrajan, A.C., Dykstra, J.E., van der Wal, A., Porada, S., 2021. Unravelling pH changes in electrochemical desalination with capacitive deionization. Environ Sci Technol 55 (20), 14165–14172. https://doi.org/10.1021/acs.est.1c04479.
[63] Dahiya, S., Singh, A., Mishra, B.K., 2021. Capacitive deionized hybrid systems for wastewater treatment and desalination: a review on synergistic effects, mechanisms and challenges. Chem Eng J 417, 128129. https://doi.org/10.1016/j.cej.2020.128129.
[64] Singh, K., Li, G., Lee, J., Zuilhof, H., Mehdi, B.L., Zornitta, R.L., de Smet, L.C.P.M., 2021. Divalent ion selectivity in capacitive deionization with vanadium hexacyanoferrate: experiments and quantum-chemical computations. Adv Funct Mater 31, 2105203. https://doi.org/10.1002/adfm.202105203.
[65] Gamaethiralalage, J.G., Singh, K., Sahin, S., Yoon, J., Elimelech, M., Suss, M.E., Liang, P., Biesheuvel, P.M., Zornitta, R.L., de Smet, L.C.P.M., 2021. Recent advances in ion selectivity with capacitive deionization. Energy Environ Sci 14, 1095–1120. https://doi.org/10.1039/D0EE03145C.
[66] Mossad, M., Zou, L., 2012. A study of the capacitive deionisation performance under various operational conditions. J Hazard Mater 213–214, 491–497. https://doi.org/10.1016/j.jhazmat.2012.02.036.
[67] Ilangovan, G., Pillai, K.C., 1997. Electrochemical and XPS characterization of glassy carbon electrode surface effects on the preparation of a monomeric molybdate(VI)-modified electrode. Langmuir 13, 566–575. https://doi.org/10.1021/la960053n.